Scaling Baroclinic Eddy Fluxes: Vortices and Energy Balance

ANDREW F. THOMPSON AND WILLIAM R. YOUNG

Scripps Institution of Oceanography, University of California, San Diego, La Jolla, California

ABSTRACT

The eddy heat flux generated by the statistically equilibrated baroclinic instability of a uniform, horizontal temperature gradient is studied using a two-mode f-plane quasigeostrophic model. An overview of the dependence of the eddy diffusivity D on the bottom friction κ, the deformation radius λ, the vertical variation of the large-scale flow U, and the domain size L is provided by numerical simulations at 70 different values of the two nondimensional control parameters $\kappa\lambda/U$ and L/λ. Strong, axisymmetric, well-separated baroclinic vortices dominate both the barotropic vorticity and the temperature fields. The core radius of a single vortex is significantly larger than λ but smaller than the eddy mixing length ℓ_{mix}. On the other hand, the typical vortex separation is comparable to ℓ_{mix}. Anticyclonic vortices are hot, and cyclonic vortices are cold. The motion of a single vortex is due to barotropic advection by other distant vortices, and the eddy heat flux is due to the systematic migration of hot anticyclones northward and cold cyclones southward. These features can be explained by scaling arguments and an analysis of the statistically steady energy balance. These arguments result in a relation between D and ℓ_{mix}. Earlier scaling theories based on coupled Kolmogorovian cascades do not account for these coherent structures and are shown to be unreliable. All of the major properties of this dilute vortex gas are exponentially sensitive to the strength of the bottom drag. As the bottom drag decreases, both the vortex cores and the vortex separation become larger. Provided that ℓ_{mix} remains significantly smaller than the domain size, then local mixing length arguments are applicable, and our main empirical result is $\ell_{\text{mix}} \approx 4\lambda \exp(0.3U/\kappa\lambda)$.

1. Introduction

Eddy heat and potential vorticity fluxes are part of a dynamical balance in which potential energy created by differential heating is released through baroclinic instability. Many theoretical and numerical studies have attempted to find physically plausible parameterizations of these eddy fluxes so that turbulent transport can be included in coarsely resolved climate models. Pioneering attempts used linear theory to describe the eddy structure and energy arguments to constrain the eddy amplitude (Green 1970; Stone 1972). More recently, though, fully nonlinear numerical realizations of homogeneous quasigeostrophic turbulence have been used to diagnose eddy fluxes in a statistical steady state maintained by imposing a uniform temperature gradient (Haidvogel and Held 1980; Hua and Haidvogel 1986;

Larichev and Held 1995; Held and Larichev 1996; Smith and Vallis 2002; Lapeyre and Held 2003). The grail is a physically motivated relation between the eddy flux of heat and control parameters, such as the imposed large-scale thermal gradient. Provided that there is scale separation between the mean and the eddies, the resulting flux–gradient relation might apply approximately to a spatially inhomogeneous flow. In other words, the hypothesis is that baroclinic eddy fluxes can be parameterized by a turbulent diffusivity D, which might, however, depend nonlinearly on the large-scale temperature gradient (e.g., Pavan and Held 1996). Our first goal in this work is largely descriptive: we characterize the dependence of D on external parameters such as the domain size L, the bottom drag coefficient κ, the Rossby deformation radius λ, and the imposed velocity jump U. Our notation is introduced systematically in appendix A and is largely the same as that of Larichev and Held (1995, hereinafter LH95): $\tau(x, y, t)$ and $\psi(x, y, t)$ are the disturbance streamfunctions of the baroclinic and barotropic modes, respectively. A precise definition of the eddy diffusivity D is

Corresponding author address: Andrew Thompson, Scripps Institution of Oceanography, University of California, San Diego, La Jolla, CA 92093-0213.
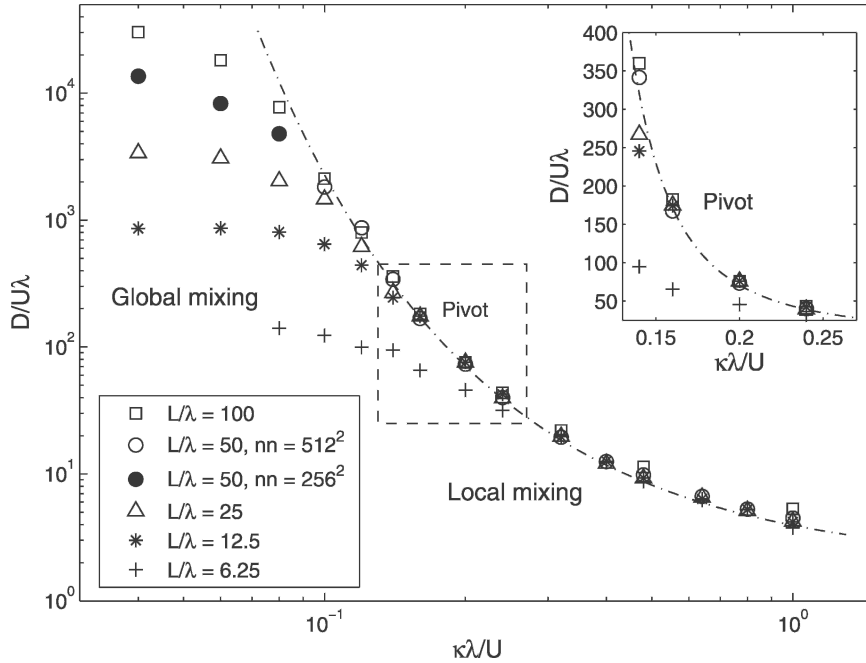E-mail: athompso@ucsd.edu

FIG. 1. A summary of eddy diffusivity, $D/U\lambda$, for 70 simulations. The smooth curve is D_{EB}^{loc} in (31). At the pivot, simulations with L/λ varying by a factor of 8 have nearly the same value of $D/U\lambda$. As summarized in Table 1, the resolution was held constant for each series of simulations, except for the series with $L/\lambda = 50$. In that series limited computer resources forced us to reduce the resolution from 512^2 (open circles) to 256^2 (filled circles) (see section 7 for details).

then

$$D \equiv U^{-1}\langle \psi_x \tau \rangle. \qquad (1)$$

Here $\langle \rangle$ denotes both a horizontal average over the square $2\pi L \times 2\pi L$ domain and an additional time average to remove residual turbulent pulsations.

In (1), $\langle \psi_x \tau \rangle$ is the product of the barotropic meridional velocity ψ_x and the thermal field τ; that is, the meridional heat flux is proportional to $\langle \psi_x \tau \rangle$. Moreover, the mechanical energy balance in a statistically steady state (see appendix A) is

$$U\lambda^{-2}\langle \psi_x \tau \rangle = \kappa \langle |\nabla \psi - \sqrt{2}\nabla \tau|^2 \rangle + \text{hyp}\nu, \qquad (2)$$

where "hypν" indicates the hyperviscous dissipation of energy. The first term on the right-hand side of (2) is the mechanical energy dissipation (watts per kilogram) by bottom drag, κ. The left-hand side of (2) is the energy extracted from the unstable horizontal temperature gradient by baroclinic instability. Enstrophy budgets also identify $\langle \psi_x \tau \rangle$ as the large-scale source balancing the hyperviscous enstrophy sink at high wavenumbers. Thus, a single quantity, conveniently defined as D in (1), summarizes all of the important quadratic power integrals and fluxes in homogeneous baroclinic turbulence.

Dimensional considerations (Haidvogel and Held 1980) show that

$$D = U\lambda \times D_* \left(\frac{\lambda}{L}, \frac{\kappa\lambda}{U}, \frac{\nu}{UL^7} \right), \qquad (3)$$

where D_* is a dimensionless function. The final argument of D_*, involving the hyperviscosity ν, is relatively small (see section 7). For brevity, we suppress reference to this hyperviscous parameter. In Fig. 1 we summarize a panoramic set of numerical simulations revealing the main features of the function $D_*(\lambda/L, \kappa\lambda/U)$. Here, D_* varies by a factor of over 1000 in response to much smaller changes in $\kappa\lambda/U$ and L/λ: there is plenty of scope for relatively crude scaling arguments to collapse this data. Finding this scaling is not entirely straightforward because there is not a convincing straight line anywhere in the log–log plot of Fig. 1. This is the first indication that the function D_* is not adequately characterized as a power law.

Classical theories of baroclinic turbulence (Rhines 1977; Salmon 1978, 1980; Haidvogel and Held 1980) argue that energy is created at large scales by differential heating and then cascades downscale to the Rossby deformation radius. Baroclinic energy is then converted
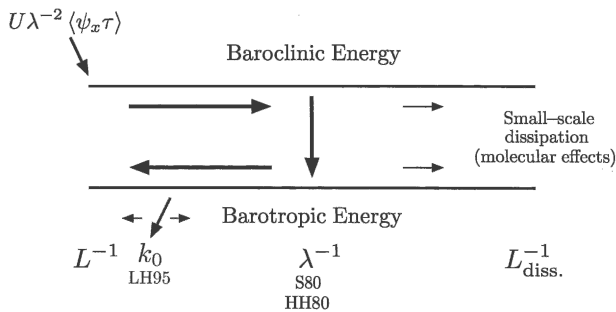
FIG. 2. Diagrammatic summary of the dual-cascade scenario (adapted from Salmon 1980, label S80 in the figure). Baroclinic energy enters the system at scales comparable to the domain size L via differential heating. Baroclinic energy is then transferred to higher wavenumbers in a direct cascade. In the classical view (S80 and HH80), energy transfers from the baroclinic to the barotropic mode at the deformation wavenumber, $k \sim \lambda^{-1}$, and barotropic energy then cascades back to larger scales and is ultimately removed by bottom drag. LH95 revised this picture by showing that the wavenumber at which energy is removed is correlated with energy production and the associated potential vorticity fluxes. LH95 identified this length scale k_0^{-1} as that of the energy-containing eddies and suggested that its location in the spectrum varied strongly with bottom drag.

to barotropic near the deformation radius, and the barotropic mode undergoes an inverse cascade until energy is removed by bottom drag. The dual-cascade scenario, summarized in Fig. 2, supposes that $L \gg \lambda$ so that there is spectral room for the cascades to operate. This regime, with the domain scale greatly exceeding the Rossby deformation radius, is also oceanographically relevant.

Early studies of baroclinic turbulence assumed that the mixing length of baroclinic eddies was comparable to λ. In these circumstances, Haidvogel and Held (1980, hereinafter HH80) argued that eddy statistics should be independent of the domain scale L. Varying the parameter L/λ between 7 and 15, HH80 provided evidence in support of this hypothesis. The data in Fig. 1 span a significantly larger range of L/λ than does HH80 and further support their conclusion that D is independent of L provided that $\kappa\lambda/U$ is not too small.

The proviso is necessary because Fig. 1 clearly shows an important distinction between two regimes: local mixing and global mixing. The local regime is exemplified by the point marked "pivot" in Fig. 1 (where $\kappa\lambda/U = 0.16$). At the pivot, four simulations with L/λ varying by a factor 8 have nearly the same D. The four pivot solutions exemplify the "local mixing regime" of HH80, within which D is independent of L. However, as $\kappa\lambda/U$ is reduced to very small values, eddy length scales grow. Once the eddy mixing length is comparable to the domain scale L, the system leaves the local mixing regime

and enters the global mixing regime, also indicated in Fig. 1.

The notion of a diffusive parameterization, applicable to a slowly varying mean flow (Pavan and Held 1996), is valid only in the local mixing regime. Thus, our main focus in the remainder of this paper is the characterization of the local regime.

Figure 3 further illustrates how modest variations of bottom drag κ greatly change the nature of the flow. HH80 and LH95 previously noted this extreme sensitivity to κ and rationalized it by arguing that bottom drag is the only mechanism preventing barotropic eddies from cascading upward, all the way to the domain scale L. Pedlosky (1983) considered the linear instability problem with bottom friction, and Riviere and Klein (1997) studied a weakly nonlinear system, but it is really the fully nonlinear studies that indicate the key role of bottom drag in equilibrated baroclinic turbulence. Smith and Vallis (2002) and Riviere et al. (2004) considered a relatively small range of κ and showed that the eddy length scale decreases with increasing bottom drag. Arbic and Flierl (2004a) presented similar results and also explored the regime $\kappa\lambda/U > 1$, where the lower-layer velocities are small. We will not consider $\kappa\lambda/U > 1$ in this paper. Arbic and Flierl (2004a) also provide evidence from current-meter data that mid-ocean eddies lie somewhere in the region $\kappa\lambda/U \approx 1$, which corresponds to the regime considered in this study.

A striking feature of the simulations is the formation and persistence of axisymmetric vortices. Figure 3 shows that the size and density of these vortices are influenced by bottom friction. The global mixing solution in Fig. 3c is dominated by just a few vortices: the volatility of the corresponding time series in Fig. 3b is due to the extreme fluctuations produced by two or three jostling vortices. It seems there is little hope of constructing a statistical theory of the few-vortex global mixing regime. The more important local regime is simpler in the sense that there are many interacting vortices: the corresponding time series in Fig. 3b is stable because of the many-vortex self-averaging. Thus, simple statistical scaling theories may have some force in the local mixing regime. Specifically, the barotropic vorticity in Fig. 3d is best characterized as a "dilute gas" of vortices (Carnevale et al. 1991). This observation, combined with some deductions based on the statistically steady energy balance in (2), provides an analytic entry exploited in sections 3 and 4.

Within the vortex cores there is a strong anticorrelation between the barotropic vorticity, $\zeta \equiv \nabla^2\psi$, and temperature τ. A cyclonic barotropic vortex traps cold fluid in its core while an anticyclonic barotropic vortex
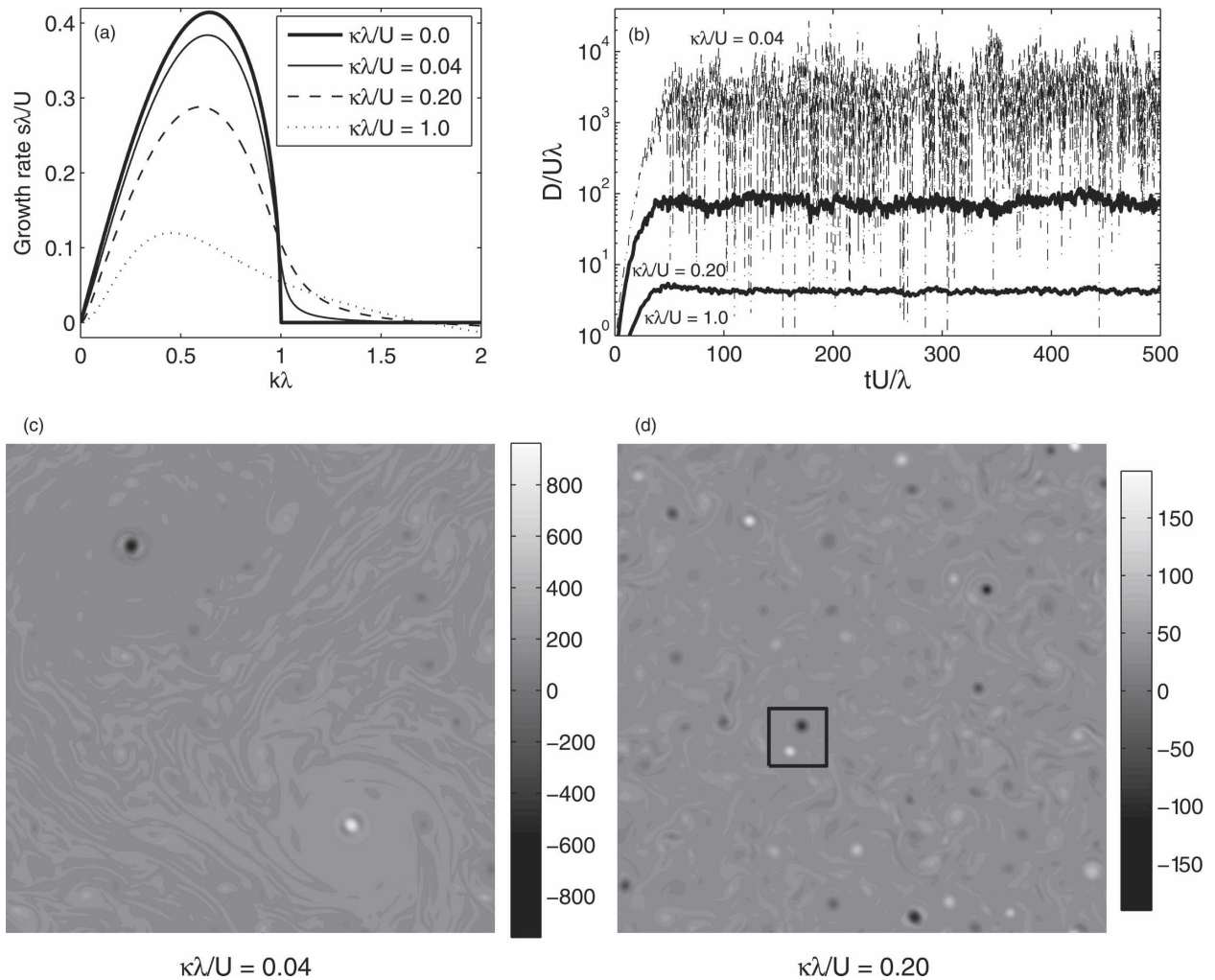
FIG. 3. (a) Growth rates of the linear baroclinic instability problem for different values of the bottom drag parameter. (b) Time series of eddy diffusivity for different values of $\kappa\lambda/U$. The "instantaneous diffusivity" shown in these time series is defined by taking $\langle\rangle$ in (1) only as an (x, y) average. (c), (d) Snapshots of the vorticity of the barotropic mode, $\nabla^2\psi\lambda/U$. In (b)–(d), $L/\lambda = 25$. The box appearing in (d) is expanded in Fig. 4.

traps warm fluid in its core. Figures 4a and 4b show expanded views of the barotropic vorticity and temperature, respectively, corresponding to the boxed region in Fig. 3d. Figure 4c shows a scatterplot of temperature and barotropic vorticity from each point in Fig. 3d. The scatterplot has a number of branches corresponding to individual vortices such as those in Figs. 4a and 4b (indicated by the gray points); therefore, most of the temperature anomaly is in the vortices. The mutual advection of these vortices is the main mechanism by which heat is transported meridionally in this system.

LH95 showed that the potential vorticity flux and the meridional heat flux (both of which are proportional to D) are dominated by the largest length scales excited by the inverse cascade. LH95 associated the length $k_0^{-1} \gg$

λ with both the mixing length and the peak of the barotropic energy spectrum. LH95 then used the dual-cascade model as a framework to derive a scaling for the diffusive parameterization of the eddy fluxes (for more detail see section 2).

However, if the bottom drag is strong enough to limit the inverse cascade to scales less than L, then arguments based on inertial energy-conserving spectral fluxes are invalid. In addition, if bottom drag is sufficiently small to allow a relatively undamped inverse cascade, then barotropic energy accumulates at the domain size, which is just the global mixing regime in Fig. 1. In Held and Larichev (1996) and Lapeyre and Held (2003), this concern is ameliorated because a planetary potential vorticity gradient β halts the inverse cascade without damping, so that the dual-cascade scenario is
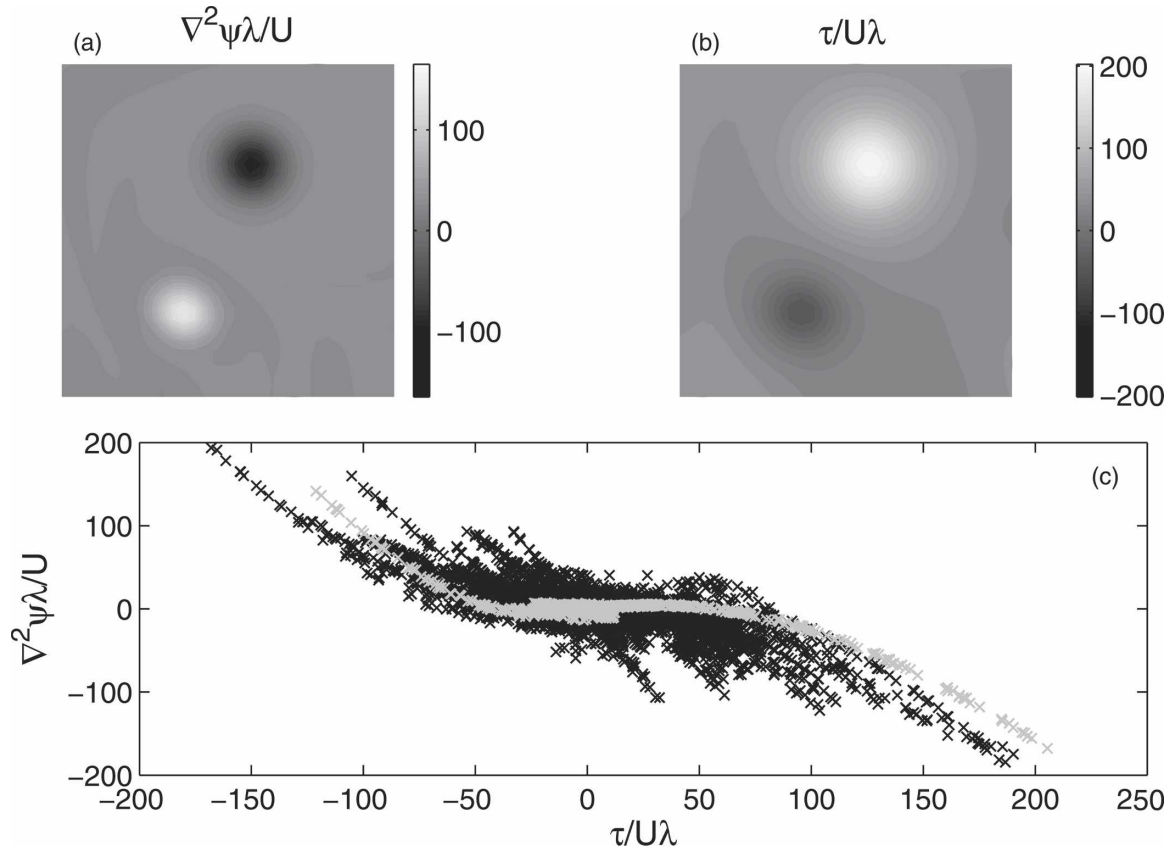
FIG. 4. Nondimensional (a) barotropic vorticity and (b) temperature from the boxed region in Fig. 3d. (c) Scatterplot of temperature and barotropic vorticity data for the snapshot in Fig. 3d. The gray points show the data that lie within the boxed region [see (a) and (b)]. The branches of the scatterplot represent individual vortices and illustrate the strong correlation between temperature and barotropic vorticity in the vortex cores.

more plausible. In the case studied here, however, with $\beta = 0$, the dual-cascade scenario is implausible. Compounding these difficulties, the dual-cascade scenario of Fig. 2 takes no explicit account of the vortices that dominate the thermal field.

For the reasons above, we reject the dual-cascade scenario, and we support this position by showing in sections 2 and 3 that the main scaling relations of the dual-cascade scenario are inaccurate. We instead argue that eddy fluxes result from the interaction of coherent baroclinic vortices. In the local mixing regime the self-averaging of these vortices allows the properties of a single "typical" vortex to be representative of domain-averaged quantities such as the turbulent diffusivity D. Therefore, in section 3 we will consider the properties of a typical vortex core. Relationships between vortex-core properties and domain-averaged values are then applied to the energy balance in section 4, which results in a scaling for D in both global and local mixing regimes. In section 5 we discuss the large-scale limit of the equations of motion and we show that there is a new

conserved quantity, the cross invariant, which characterizes the anticorrelation between τ and ζ. In section 6 we present an empirical formula that collapses the results of the simulations. Section 7 discusses the sensitivity of the numerical results to hyperviscosity and resolution, and section 8 is the discussion and conclusions. Appendix A summarizes our notation and the two-mode quasigeostrophic equations, and in appendix B we describe an automated vortex census algorithm used to verify our vortex-scaling assumptions.

2. Large eddies and dual-cascade scaling

LH95 performed large-domain simulations with $L/\lambda = 50$, which for the first time allowed the inverse cascade in the barotropic mode to be observed. Analyzing spectral representations of baroclinic and barotropic energy levels, LH95 found that energy production is localized at length scales much larger than the Rossby deformation radius λ. On the other hand, energy transfer from the baroclinic to the barotropic mode near λ
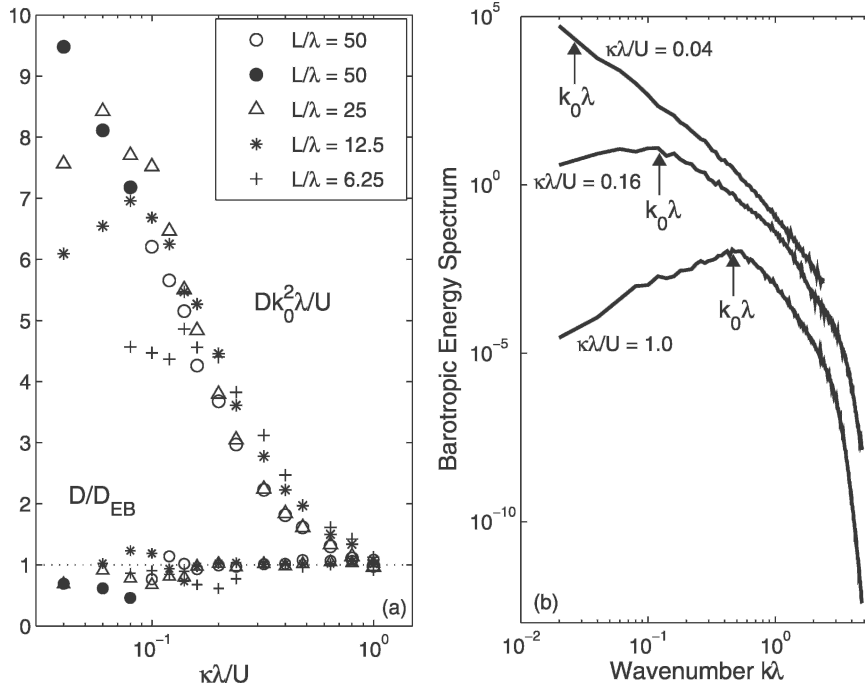
FIG. 5. (a) A comparison of the dual-cascade prediction, $D_{DC} \sim U/k_0^2\lambda$, with the simulated Ds. Also shown is the ratio of the simulated D to D_{EB} defined in (31) for the local mixing regime. Points within the global mixing regime use (29) with $\ell_{mix} = \pi L$. (b) A comparison of the length scale k_0^{-1}, defined in (6), with the LH95 definition of the energy-containing length, which is identified with the largest energy-containing wavenumber of the barotropic mode. The LH95 definition and our definition are in good agreement.

plays the passive, but important, role of energizing the inverse cascade. LH95 then proposed a revision to the theory of HH80 and Salmon (1980) by arguing that the appropriate mixing length should be k_0^{-1}, not λ. LH95 identified k_0 as the wavenumber corresponding to the peak in the barotropic energy spectrum; that is, k_0 is both the wavenumber of the energy-containing eddies and the inverse of the mixing length. This modification of the dual-cascade scenario is indicated in Fig. 2 by the arrow labeled LH95. Figure 2 also indicates that the exact location of k_0 along the barotropic spectrum can vary dramatically due to a strong dependence on bottom friction.

LH95 then proceeded to estimate the eddy diffusivity as

$$D = \text{characteristic barotropic velocity } V$$
$$\times \text{ mixing length.} \qquad (4)$$

Retaining the dual-cascade scenario as an interpretative framework, and taking k_0^{-1} as the mixing length, LH95 argue that $V \sim U/k_0\lambda$. Thus, once the dust settles, the final result is the dual-cascade scaling

$$D_{DC} \sim U/k_0^2\lambda. \qquad (5)$$

The strong dependence of D_{DC} on bottom drag κ is im-

plicit in k_0, but no relationship between k_0 and κ was proposed by LH95.

In Fig. 5 we test the scaling (5) using the data in Fig. 1 and the definition

$$k_0 \equiv \sqrt{\langle|\nabla\psi|^2\rangle/\langle\psi^2\rangle}. \qquad (6)$$

Figure 5b shows that k_0 defined in (6) corresponds well to the peak in the barotropic energy spectrum in both the local and global mixing regimes. We also found that k_0 defined in (6) is insensitive to changes in the hyperviscosity and numerical resolution.

If the scaling in (5) is valid, then the nondimensional ratio $D\lambda k_0^2/U$ in Fig. 5a should be a constant, independent of both $\kappa\lambda/U$ and L/λ. Instead, $D\lambda k_0^2/U$ varies by a factor of 10. Our conclusion is that (5) has little value as a correlation between eddy diffusivity D and the peak wavenumber of the barotropic energy spectrum, k_0. It is perhaps not surprising that a length scale associated with the barotropic energy spectrum gives poor quantitative agreement in a flow dominated by baroclinic vortices.

One reason behind the failure of (5) is the assumption that k_0^{-1} is equivalent to the mixing length. A more precise definition of the mixing length is
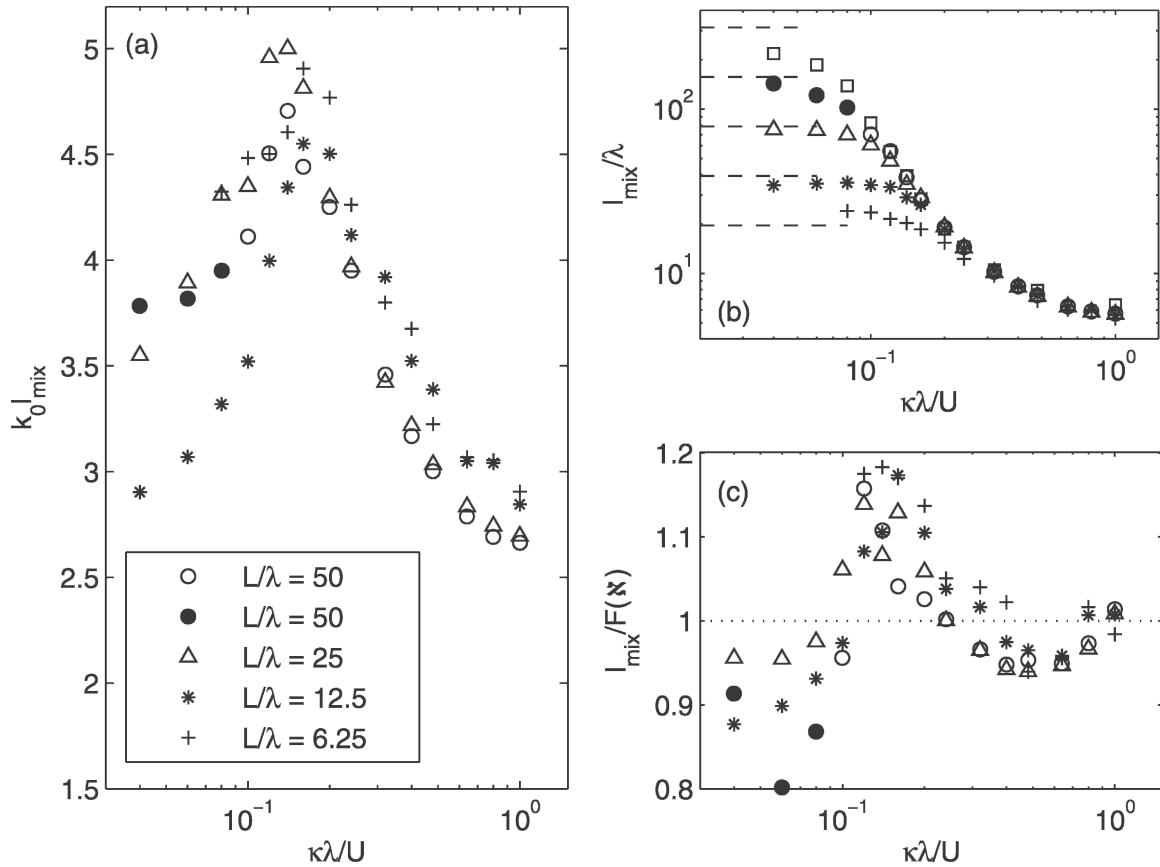
FIG. 6. (a) A comparison of k_0^{-1}, the LH95 length scale associated with the largest energy-containing eddies, and ℓ_{mix}, our mixing length defined in (7). (b) A survey of ℓ_{mix}/λ values showing the statistical independence of domain size at moderate values of $\kappa\lambda/U$. The dashed lines indicate $\pi L/\lambda$. (c) A comparison of the observed mixing length with the empirical fit proposed in (37).

$$\ell_{mix} \equiv U^{-1}\sqrt{\langle\tau^2\rangle}. \qquad (7)$$

According to this definition, ℓ_{mix} times the basic-state τ gradient, U, is equal to the root-mean-square fluctuation, $\sqrt{\langle\tau^2\rangle}$. This definition of the mixing length is consistent with the large-scale limit of the governing equations in which the baroclinic evolution equation reduces to the advection of the quasi-passive scalar τ by the barotropic flow (see section 5).

Figure 6a shows that the nondimensional number $k_0\ell_{mix}$ varies by over a factor of 2. Moreover, $k_0\ell_{mix}$ has a maximum value as a function of $\kappa\lambda/U$. This peak in $k_0\ell_{mix}$ is the clearest demarcation between the local and global mixing regimes in our simulations.[1] This peak arises because ℓ_{mix} reaches the domain size (and saturates) at a smaller value of $\kappa\lambda/U$ than does the energy-

---

[1] Both Figs. 1 and 6a show that the value of $\kappa\lambda/U$ at which the local to global transition occurs depends on L/λ. At $L/\lambda = 50$, the peak in $k_0\ell_{mix}$ is roughly $\kappa\lambda/U = 0.1$ At $L/\lambda = 25$, the peak is at 0.16.

containing length scale, k_0^{-1}. Further discussion of these two length scales appears in section 8. Figure 6b shows ℓ_{mix}/λ as a function of $\kappa\lambda/U$. The dashed lines at the left are $\pi L/\lambda$ and indicate that ℓ_{mix} saturates at about πL, or one-half of the domain size, as $\kappa\lambda/U \to 0$. In the local mixing regime, the eddy diffusivity D is independent of domain size L, and Fig. 6b shows that the ratio ℓ_{mix}/λ shares this independence.

Following the expression for D in (4), we also write the diffusivity in terms of the eddy mixing length and the meridional barotropic velocity V. We define

$$V \equiv \sqrt{\langle\psi_x^2\rangle}, \qquad (8)$$

and we introduce the correlation coefficient

$$c \equiv \frac{\langle\psi_x\tau\rangle}{\sqrt{\langle\psi_x^2\rangle\langle\tau^2\rangle}}, \qquad (9)$$

so that $D = cV\ell_{mix}$. To examine this relationship we show the correlation c in Fig. 7. In the local regime, c has a weak dependence on $\kappa\lambda/U$: the dashed line in Fig.
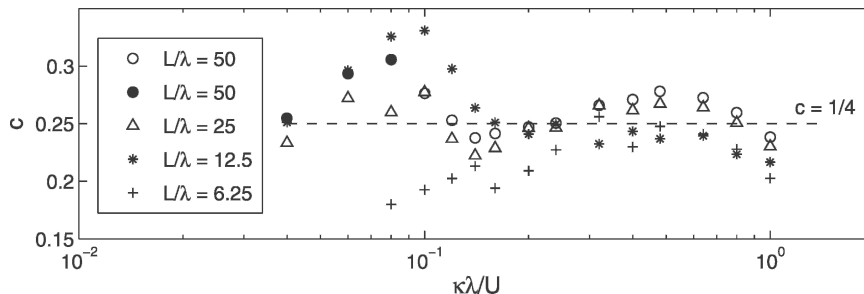
FIG. 7. A survey of the correlation coefficient c as defined in (9). Within the local mixing regime c is approximately equal to 1/4.

7 indicates that $c \approx 1/4$. Taking c to be constant, then, throughout the local mixing regime, an important scaling relation[2] is

$$D \sim V\ell_{\mathrm{mix}}. \tag{10}$$

3. Vortex properties in the local mixing regime

To this point we have introduced three diagnostics characterizing the domain-averaged flow—namely, D, ℓ_{mix}, and V. We now consider the vortices themselves and relate vortex-core properties to D, ℓ_{mix}, and V. We employ three important scaling assumptions that are valid in the local mixing regime:

1) Temperature τ and barotropic vorticity ζ are dominated by the vortex cores; τ_{core} and ζ_{core} denote typical core values.
2) A typical core radius r_{core} is significantly greater than λ, and core barotropic potential vorticity scales with the core baroclinic potential vorticity, that is, $\zeta_{\mathrm{core}} \sim \lambda^{-2}\tau_{\mathrm{core}}$.
3) The value of ℓ_{mix} scales with the typical spacing between vortices, and the total number of vortices $\sim (L/\ell_{\mathrm{mix}})^2$.

The three assumptions are supported by diagnosis of the simulations. Assumption 2 is a result of total potential vorticity conservation; assumption 2 is also supported by the scatterplot in Fig. 4c.

We consider the flow to be a dilute vortex gas. Since the temperature field is dominated by the vortex cores, the squared temperature fluctuation $\langle \tau^2 \rangle$ should scale with τ^2 integrated over a single vortex core, that is $\tau_{\mathrm{core}}^2 r_{\mathrm{core}}^2$, multiplied by the number of vortices in the

domain, $L^2/\ell_{\mathrm{mix}}^2$, and finally divided by L^2 to form the average. Using the definition of ℓ_{mix} in (7) we can thus write τ_{core} in terms of the two length scales ℓ_{mix} and r_{core} as

$$\tau_{\mathrm{core}} \sim \frac{U\ell_{\mathrm{mix}}^2}{r_{\mathrm{core}}}. \tag{11}$$

We turn now to the second assumption, $\zeta_{\mathrm{core}} \sim \tau_{\mathrm{core}}/\lambda^2$, and eliminate τ_{core} using (11). This gives

$$\zeta_{\mathrm{core}} \sim \frac{U\ell_{\mathrm{mix}}^2}{\lambda^2 r_{\mathrm{core}}}. \tag{12}$$

Next, following Carnevale et al. (1991), and using the estimate in their (3), we relate the barotropic velocity V to the core vorticity by $V \sim \zeta_{\mathrm{core}} r_{\mathrm{core}}^2/\ell_{\mathrm{mix}}$. Eliminating ζ_{core} with (12) one has

$$V \sim \frac{U\ell_{\mathrm{mix}} r_{\mathrm{core}}}{\lambda^2}. \tag{13}$$

From (10) one now obtains the eddy diffusivity in terms of r_{core} and ℓ_{mix}:

$$D \sim \frac{U\ell_{\mathrm{mix}}^2 r_{\mathrm{core}}}{\lambda^2}. \tag{14}$$

It is intriguing that the scaling relations above imply that $D \sim \zeta_{\mathrm{core}} r_{\mathrm{core}}^2$, that is, that the circulation of a typical vortex scales with the eddy diffusivity.

To test (11)–(14) we need r_{core}. The most precise way to obtain the typical vortex radius r_{core} is to identify individual vortices and measure each r_{core} according to some objective definition. A faster and more convenient alternative is to again use vortex-scaling theory and estimate $\langle \zeta^2 \rangle$ as ζ^2 integrated over a single vortex core, that is, $\zeta_{\mathrm{core}}^2 r_{\mathrm{core}}^2$, multiplied by the number of vortices in the domain, $L^2/\ell_{\mathrm{mix}}^2$, and finally divided by L^2 to form the average. This gives $\langle \zeta^2 \rangle \sim (\zeta_{\mathrm{core}} r_{\mathrm{core}}/\ell_{\mathrm{mix}})^2$. Using (12) and (13) this implies that $r_{\mathrm{core}} \sim V/\sqrt{\langle \zeta^2 \rangle}$.

---

[2] Here, $A \sim B$ ("A scales with B") means that the ratio A/B is approximately constant as the control parameters $\kappa\lambda/U$ and L/λ vary. In practical terms "approximately constant" means that A/B varies by $\pm 20\%$; e.g., (10) is true in the local mixing regime since $D = (0.25 \pm 0.05)V\ell_{\mathrm{mix}}$.
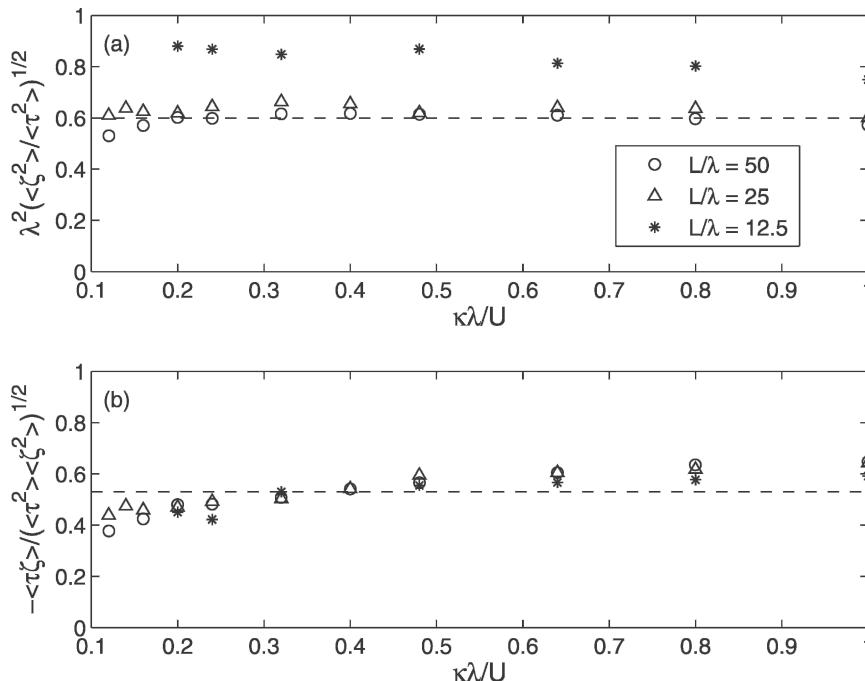
FIG. 8. A survey of the two constant ratios (a) $\varkappa_1 \equiv \lambda^2 \sqrt{\langle \zeta^2 \rangle} / \sqrt{\langle \tau^2 \rangle}$ and (b) $\varkappa_1 \equiv \langle \tau \zeta \rangle / \sqrt{\langle \tau^2 \rangle \langle \zeta^2 \rangle}$. Here, $\varkappa_1$ varies slightly because of resolution differences between L/λ series (see section 7). The dashed lines indicate $\varkappa_1 \approx 0.60$ and $\varkappa_2 \approx 0.53$. The data shown here focus on the local mixing regime. Results from some simulations are unavailable because $\langle \zeta^2 \rangle$ was not collected in the original suite of simulations.

These considerations motivate the definition of a new length ℓ_ζ as

$$\ell_\zeta \equiv \sqrt{\frac{V^2}{\langle \zeta^2 \rangle}}, \qquad (15)$$

and the scaling hypothesis

$$r_{\text{core}} \sim \ell_\zeta. \qquad (16)$$

Here ℓ_ζ is simply an easily diagnosed surrogate for r_{core}.

Invoking (16), we can replace r_{core} by ℓ_ζ in (11)–(14). In particular from (13) the vortex-scaling theory predicts that the ratio

$$\varkappa_1 \equiv \frac{V \lambda^2}{U \ell_{\text{mix}} \ell_\zeta} = \frac{\lambda^2 \sqrt{\langle \zeta^2 \rangle}}{\sqrt{\langle \tau^2 \rangle}} \qquad (17)$$

is constant. We see in Fig. 8a that this ratio is indeed remarkably constant although there is variation in the value of $\varkappa_1$ because of resolution differences (for further discussion see section 7). These variations do not have a large effect on our estimates for D in the following sections, and for the purposes of making quantitative estimates we will take $\varkappa_1$ to be approximately 0.60 (the $L/\lambda = 25$ and 50 series). Another indication of the vortex gas scaling is that the ratio

$$\varkappa_2 \equiv - \frac{\langle \tau \zeta \rangle}{\sqrt{\langle \tau^2 \rangle \langle \zeta^2 \rangle}} \qquad (18)$$

is also roughly constant and equal to 0.53, independent of resolution effects; see Fig. 8b.

To further verify our vortex-scaling theory, we use an automated "vortex census" to quantify vortex statistics in simulations at seven different values of $\kappa \lambda / U$. In Fig. 9 we provide confirmation of the two relationships prominently involving the length scales ℓ_{mix} and r_{core}. In Fig. 9a, we plot the mean number of vortices, N, for each value of $\kappa \lambda / U$. Here, N is determined from 50 snapshots of the barotropic vorticity field in its equilibrated turbulent state. Vortex theory predicts $\ell_{\text{mix}} \sim N^{-1/2}$ and our vortex census shows that $\ell_{\text{mix}} \sim N^{-0.57 \pm 0.05}$. The variation in the exponent is due to changes in the vortex census parameters. These parameters and the vortex census algorithm are described in appendix B. Figure 9b plots the ratio $l_\zeta / r_{\text{core}}$, where r_{core} is determined from the vortex census. The ratio is constant to within $\pm 10\%$ although the observed $l_\zeta / r_{\text{core}}$ does systematically increase as $\kappa \lambda / U$ decreases. The core radius is difficult to quantify because typical vortices only span three to six grid spaces for these large-domain simulations. Still, the results in Figs. 8 and 9
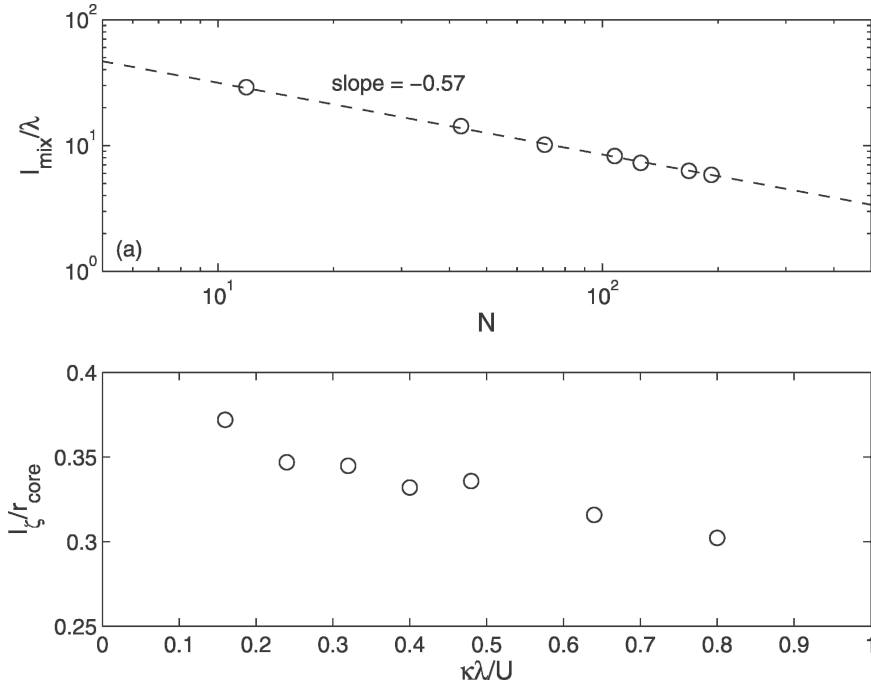
FIG. 9. (a) The number of vortices N in the equilibrated turbulent state for seven different values of $\kappa\lambda/U$ as determined from an automated vortex census. Smaller values of $\kappa\lambda/U$ correspond to fewer vortices and a larger mixing length; vortex theory predicts $\ell_{\mathrm{mix}} \sim N^{-1/2}$. (b) Ratio of l_ζ, defined in (15), to r_{core}, as determined by the vortex census, at the same seven values of $\kappa\lambda/U$. The ratio is constant to within $\pm10\%$. A description of the vortex census algorithm is given in appendix B.

give us confidence that the assumptions made at the outset of this section are indeed true: in the local mixing regime there is a self-similar population of vortices.

To conclude this section we notice that (17) can be rearranged as

$$\frac{V\lambda}{U\ell_{\mathrm{mix}}} \approx 0.60 \times \frac{\ell_\zeta}{\lambda}. \tag{19}$$

The dual-cascade scenario argues that direct and inverse cascade rates are equal and thus predicts the ratio $V\lambda/U\ell_{\mathrm{mix}}$ is constant. Equivalently, the large-scale eddy turnover time, ℓ_{mix}/V, is equal to the linear baroclinic instability growth rate λ/U. However, we show in the next section that the right-hand side of (19) is actually a nonconstant function of $\kappa\lambda/U$; see (26). Diagnosis of the simulations confirms both (19) and (26).

4. The energy balance

In the previous sections we introduced six unknown quantities: r_{core} (or equivalently ℓ_ζ), τ_{core}, ζ_{core}, D, V, and ℓ_{mix}. We regard the first and last as the most basic quantities and in (11)–(14) we have expressed the middle four in terms of these. A final relationship that

we have yet to exploit is the statistically steady energy balance in (2). This provides a fifth relation between the six unknowns (r_{core}, τ_{core}, ζ_{core}, D, V, and ℓ_{mix}).

Neglecting hyperviscosity, we can expand the energy balance in (2) to write

$$U\lambda^{-2}\langle\psi_x\tau\rangle \approx \kappa(\langle|\nabla\psi|^2\rangle - 2\sqrt{2}\langle\nabla\psi\cdot\nabla\tau\rangle + 2\langle|\nabla\tau|^2\rangle). \tag{20}$$

Diagnostics show that within the local regime the three terms on the right-hand side of (20) are comparable.[3]

The definitions in (1) and (8) and the fact that the flow is largely isotropic allow us to first rewrite the energy balance as

$$\frac{U^2}{\lambda^2} D \approx \kappa(2V^2 - 2\sqrt{2}\langle\nabla\psi\cdot\nabla\tau\rangle + 2\langle|\nabla\tau|^2\rangle). \tag{21}$$

Using integration by parts, the quantity $\langle\nabla\psi\cdot\nabla\tau\rangle$, which we will refer to as the cross invariant, can be

---

[3] The global mixing regime is much simpler because the Ekman dissipation is dominated by the barotropic mode: $\varepsilon_{\mathrm{Ekman}} \approx \kappa\langle|\nabla\psi|^2\rangle$.
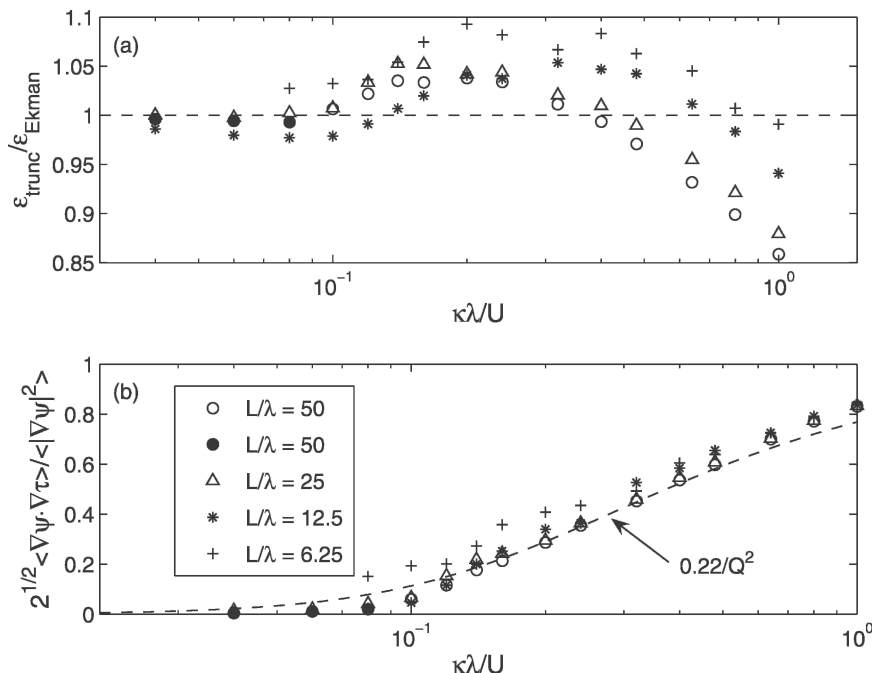
FIG. 10. (a) The ratio of the truncated dissipation $\varepsilon_{\text{trunc}} = \kappa(\langle|\nabla\psi|^2\rangle - \sqrt{2}\langle\nabla\psi \cdot \nabla\tau\rangle)$ to the total Ekman dissipation $\varepsilon_{\text{Ekman}} = \kappa(\langle|\nabla\psi - \sqrt{2}\nabla\tau|^2\rangle)$. (b) The ratio of the two terms composing $\varepsilon_{\text{trunc}}$. One can show from (17), (22), and (26) that vortex-scaling theory predicts this ratio to be approximately $\sqrt{2}\varkappa_1\varkappa_2/2Q_*^2$, where $Q(\kappa_*)$ is defined in (27). The dashed line shows that there is good agreement between theory and the simulations. In the global mixing regime, $\varepsilon_{\text{trunc}} \approx \langle|\nabla\psi|^2\rangle$.

rewritten as $-\langle\tau\zeta\rangle$. Both temperature and barotropic vorticity are dominated by values in the vortex cores; therefore, the product $\tau\zeta$ is strongly dominated by core values. Thus, returning to our vortex-core relations from section 3, and specifically using (18) with the definitions of ℓ_{mix} and ℓ_ζ in (7) and (15), we can write

$$-\langle\tau\zeta\rangle = \varkappa_2 UV \frac{\ell_{\text{mix}}}{\ell_\zeta}, \qquad (22)$$

where $\varkappa_2 \approx 0.53$. Note that the negative sign is necessary on the left-hand side of (22) because τ and ζ are negatively correlated. This strong anticorrelation between τ and ζ is important because the cross term makes a significant contribution to the dissipation in (20).

The final term on the right-hand side of (20) involves $\langle|\nabla\tau|^2\rangle$. Unfortunately, $\langle|\nabla\tau|^2\rangle$ cannot be directly related to the vortex-core properties because the domain average of the temperature *gradient* fluctuations is not dominated by vortex cores. Instead, equal contributions to this average come from the vortex cores and the surrounding filamentary sea. In the sea between the vortices, τ suffers a cascade to small scales and $|\nabla\tau|$ can

become comparable to typical core values. The nonvortex contribution to $\langle|\nabla\tau|^2\rangle$ is further enhanced because the filamentary sea accounts for a much larger percentage of the domain than do the vortices.

The first hope then is that $\langle|\nabla\tau|^2\rangle$ is small relative to the other terms in (20). But diagnosis shows that this is not the case in the local mixing regime. Not only does $\langle|\nabla\tau|^2\rangle$ make an important contribution, but a surprisingly good approximation in the local mixing regime is that

$$\sqrt{2}\langle|\nabla\tau|^2\rangle \approx \langle\nabla\psi \cdot \nabla\tau\rangle. \qquad (23)$$

That is, $\langle|\nabla\tau|^2\rangle$ cancels almost exactly one-half of the cross term, so that the total dissipation on the right-hand side of (20) can be approximated by $\kappa(\langle|\nabla\psi|^2\rangle - \sqrt{2}\langle\nabla\psi \cdot \nabla\tau\rangle)$. Figure 10a shows the ratio of this truncated dissipation $\varepsilon_{\text{trunc}}$ to the total dissipation due to Ekman friction $\varepsilon_{\text{Ekman}}$ for 60 simulations. For most of parameter space, the truncated dissipation is accurate to within $\pm 5\%$ of the total Ekman dissipation. To understand why the approximation in (23) is so accurate, we must consider the large-scale limit of the governing equations and conservation of the cross invariant in section 5.

Returning to the energy balance in (21), and applying the approximations in (22) and (23), we have

$$\frac{U^2}{\lambda^2} D \approx \kappa \left(2V^2 - \sqrt{2}\varkappa_2 UV \frac{\ell_{\mathrm{mix}}}{\ell_\zeta} \right). \qquad (24)$$

If we first replace D with $cV\ell_{\mathrm{mix}}$ and then multiply (24) by a factor of $\lambda^3/U^3\ell_{\mathrm{mix}}^2$, we find that each of the three terms is proportional to some power of $V\lambda/U\ell_{\mathrm{mix}}$. From (17), this ratio is equivalent to $\varkappa_1\ell_\zeta/\lambda$. These steps reduce (24) to the quadratic equation

$$2\kappa_* \left(\varkappa_1 \frac{\ell_\zeta}{\lambda} \right)^2 - c \left(\varkappa_1 \frac{\ell_\zeta}{\lambda} \right) - \sqrt{2}\kappa_*\varkappa_1\varkappa_2 \approx 0, \qquad (25)$$

where $\kappa_* = \kappa\lambda/U$, the nondimensional bottom friction. Solving (25) and choosing the positive root gives

$$\varkappa_1 \frac{\ell_\zeta}{\lambda} \approx Q(\kappa_*), \qquad (26)$$

where

$$Q(\kappa_*) \equiv \frac{1}{2} \left(\frac{c}{2\kappa_*} + \sqrt{\frac{c^2}{4\kappa_*^2} + 2\sqrt{2}\varkappa_1\varkappa_2} \right),$$

$$= \frac{1}{2} \left(\frac{1}{8\kappa_*} + \sqrt{\frac{1}{64\kappa_*^2} + 0.9} \right). \qquad (27)$$

In the second expression the numerical values are obtained using $c = 0.25$, $\varkappa_1 = 0.60$, and $\varkappa_2 = 0.53$.

The goal is to find a scaling for D, so we return to $D = cV\ell_{\mathrm{mix}}$, and express V in terms of ℓ_ζ and ℓ_{mix} using (17). With $c = 1/4$ this leads to

$$D \approx \frac{U\ell_{\mathrm{mix}}^2}{4\lambda} \times \left(\varkappa_1 \frac{\ell_\zeta}{\lambda} \right), \qquad (28)$$

or using (26)

$$D \approx \frac{U\ell_{\mathrm{mix}}^2}{8\lambda} \left(\frac{1}{8\kappa_*} + \sqrt{\frac{1}{64\kappa_*^2} + 0.9} \right). \qquad (29)$$

A complete expression for D solely in terms of external parameters requires another relation connecting ℓ_{mix} to known quantities. Unfortunately, we have not found a physical argument for this relationship. Instead in section 6 we propose an empirical fit for ℓ_{mix}. The main result obtained from those empirical considerations is that in the local regime

$$\ell_{\mathrm{mix}}^{\mathrm{loc}} \approx 4\lambda \exp\left(\frac{3U}{10\kappa\lambda} \right), \qquad (30)$$

[see (38) and the surrounding discussion]. Eliminating ℓ_{mix} from (29) using (30) gives the energy-balance scaling, $D \approx D_{\mathrm{EB}}^{\mathrm{loc}}$, where

$$D_{\mathrm{EB}}^{\mathrm{loc}} = 2 \exp\left(\frac{3}{5\kappa_*} \right) \left(\frac{1}{8\kappa_*} + \sqrt{\frac{1}{64\kappa_*^2} + 0.9} \right) U\lambda. \qquad (31)$$

This equation is the smooth curve in Fig. 1. Furthermore, Fig. 5a shows the ratio of the simulated D to D_{EB} within the local mixing regime. For data within the global mixing regime, ℓ_{mix} is set equal to πL in (29). The ratio is close to unity in the local mixing regime, and even does reasonably well in the global mixing regime where c, $\varkappa_1$, and $\varkappa_2$ are variable. Further discussion of the transition from local to global mixing appears in section 6.

5. The large-scale limit and the cross invariant

Our analysis of the energy balance equation in section 4 relies crucially on the approximation (23), which enables us to relate $\langle |\boldsymbol{\nabla}\tau|^2 \rangle$ to vortex properties. To understand this approximation we consider the large-scale, slow-time limit of the equations of motion, that is, the dynamics on length scales much greater than λ. To extract this limit we first nondimensionalize length with λ and time with λ/U. Then if $\varepsilon \equiv \lambda/\ell_{\mathrm{mix}} \ll 1$, one obtains the large-scale limit with $\partial_x \to \varepsilon\partial_x$ and $\partial_t \to \varepsilon\partial_t$. To retain the proper balance of terms, the amplitudes of ψ and τ are boosted by a factor of $1/\varepsilon$. The result of this maneuver is the scaled evolution equations:

$$\nabla^2\psi_t + J(\psi, \nabla^2\psi) + J(\tau, \nabla^2\tau) + \nabla^2\tau_x = -\frac{\kappa_*}{\epsilon}\nabla^2(\psi - \sqrt{2}\tau) + O(\epsilon^2) \qquad (32)$$

and

$$\tau_t + J(\psi, \tau) - \psi_x = \sqrt{2}\epsilon\kappa_*\nabla^2(\sqrt{2}\tau - \psi) + O(\epsilon^2), \qquad (33)$$

where $\kappa_* = \kappa\lambda/U$. The left-hand sides of (32) and (33) are familiar from earlier studies of large-scale quasigeostrophic turbulence (Salmon 1980; LH95). The right-hand sides of (32) and (33) reveal the large-scale effects of bottom friction. In (32) the $O(\varepsilon^{-1}\kappa_*)$ dissipative terms on the right are significant, if not dominant, depending on the size of κ_*. Notice also that the largest coupling of ψ into (33) is due to bottom friction, rather than the $O(\varepsilon^2)$ nonlinear terms.

If $\kappa_* = O(1)$, we must have $\psi - \sqrt{2}\tau = O(\epsilon)$ to control the ε^{-1} term on the right of (32). This is Arbic and Flierl's (2004a) equivalent barotropic flow, where

the lower layer is almost spun down.[4] Roughly speaking, $\psi - \sqrt{2}\tau = O(\epsilon)$ is characteristic of most of the local regime. We resisted this conclusion and attempted to control the ε^{-1} term on the right of (32) by making κ_* sufficiently small. But this victory is pyrrhic because once $\kappa_*/\varepsilon = O(1)$ the system is in the global regime. Thus, in the local regime, where the concept of an eddy diffusivity is relevant, the bottom friction is always problematic in the large-scale barotropic vorticity equation in (32). This is a fundamental reason for the failure of the dual-cascade theory.

The nonlinear terms in (32) and (33) conserve the cross invariant:

$$\langle \boldsymbol{\nabla}\psi \cdot \boldsymbol{\nabla}\tau \rangle = -\langle \tau\zeta \rangle. \tag{34}$$

The motivation for studying the cross invariant comes from the strong anticorrelation between τ and ζ within the vortex cores. To obtain the cross-invariant conservation law, multiply (32) by τ and (33) by ζ and add the results. Averaging over space, one finds that to leading order

$$\frac{\partial}{\partial t}\langle \tau\zeta \rangle = \frac{\kappa_*}{\epsilon}\left(\langle \boldsymbol{\nabla}\psi \cdot \boldsymbol{\nabla}\tau \rangle - \sqrt{2}\langle |\boldsymbol{\nabla}\tau|^2 \rangle\right). \tag{35}$$

We emphasize that (35) is a new conservation law of the large-scale dynamics—there is no clear relation between (35) and the energy and enstrophy conservation laws of the full system. Now in statistical steady state, there can be no net production of the cross invariant $\langle \tau\zeta \rangle$. This requires that the right-hand side of (35) is zero (or take a time average). This prediction is well verified in the simulations, and crucial in simplifying

the energy balance equation in section 4 [see (23) and subsequent discussion].

6. Empirical expressions for the mixing length

To eliminate the mixing length from (29) we need to express ℓ_{mix} in terms of external parameters. We are unable to find a satisfactory physical argument and instead we indulge in some curve fitting. In Fig. 6b, ℓ_{mix} has an independent dependence on two dimensionless parameters, L/λ and $\kappa\lambda/U$. We found empirically that the introduction of the combination $\aleph$, defined by

$$\aleph \equiv \frac{3}{10}\frac{U}{\kappa\lambda} - \ln\left(\frac{\pi L}{4\lambda}\right), \tag{36}$$

collapses the data in both the local and global regimes (see Fig. 11).

The definition (36) is constructed so that $\aleph = 0$ is roughly the border between local and global mixing. The factor 3/10 is a simple fraction that best collapses the ℓ_{mix} data in the local mixing regime. The combination $\aleph$ accounts for the observation that for increasing L/λ, the global–local transition occurs at smaller and smaller values of $\kappa\lambda/U$. However, the dependence is very weak, and this motivates the logarithm of L/λ in (36).

Using $\aleph$, we propose the empirical formula

$$\ell_{\mathrm{mix}} \approx \pi L \frac{e^{\aleph}}{\sqrt{1 + e^{2\aleph}}} \equiv \pi L\,\mathcal{F}(\aleph). \tag{37}$$

Figure 6c shows that (37) collapses the ℓ_{mix} data. Equation (37) is constructed so that

$$\ell_{\mathrm{mix}} \approx \begin{cases} \pi L, & \text{in the global regime, } e^{2\aleph} \gg 1, \\ \pi L \exp(\aleph) = 4\lambda \exp(3U/10\kappa\lambda), & \text{in the local regime, } e^{2\aleph} \ll 1. \end{cases} \tag{38}$$

In the global mixing regime ℓ_{mix} saturates at πL, or roughly half the domain size. In the local regime ℓ_{mix} is independent of L and exponentially sensitive to $\kappa\lambda/U$.

It is our consistent experience that this exponential dependence of ℓ_{mix} on $U/\kappa\lambda$ is more convincing than a power law in the local regime. For example, the ℓ_{mix}/L points in Fig. 11 fall cleanly on the straight line corresponding to $e^{\aleph}$. This observation is the most compelling motivation for the introduction of $e^{\aleph}$ in (37) and (38).

In the local mixing regime the vortex-scaling theory in (13) and (14) predicts that $V \propto r_{\mathrm{core}}\ell_{\mathrm{mix}}$ and D

$\propto r_{\mathrm{core}}\ell_{\mathrm{mix}}^2$. Since $r_{\mathrm{core}} \sim \ell_{\zeta} \propto Q(\kappa_*)$ we can eliminate the dependence on r_{core} by considering V/Q and D/Q, where $Q(\kappa_*)$ is defined in (27). Thus, in the local mixing regime vortex scaling predicts that

$$\frac{V}{Q} \propto \ell_{\mathrm{mix}} \propto e^{\aleph} \tag{39}$$

and

$$\frac{D}{Q} \propto \ell_{\mathrm{mix}}^2 \propto e^{2\aleph}. \tag{40}$$

Figure 11 shows the ratios above plotted against $\aleph$. The straight lines in the local regime ($\aleph < 0$) further confirm the vortex scaling. Figure 11 also shows that all the

---

[4] Notice that if ψ is precisely proportional to τ, then the energy production $\langle \psi_x \tau \rangle$ also precisely vanishes. Thus, the residual $\psi - \sqrt{2}\tau$ is certainly nonzero and very important.
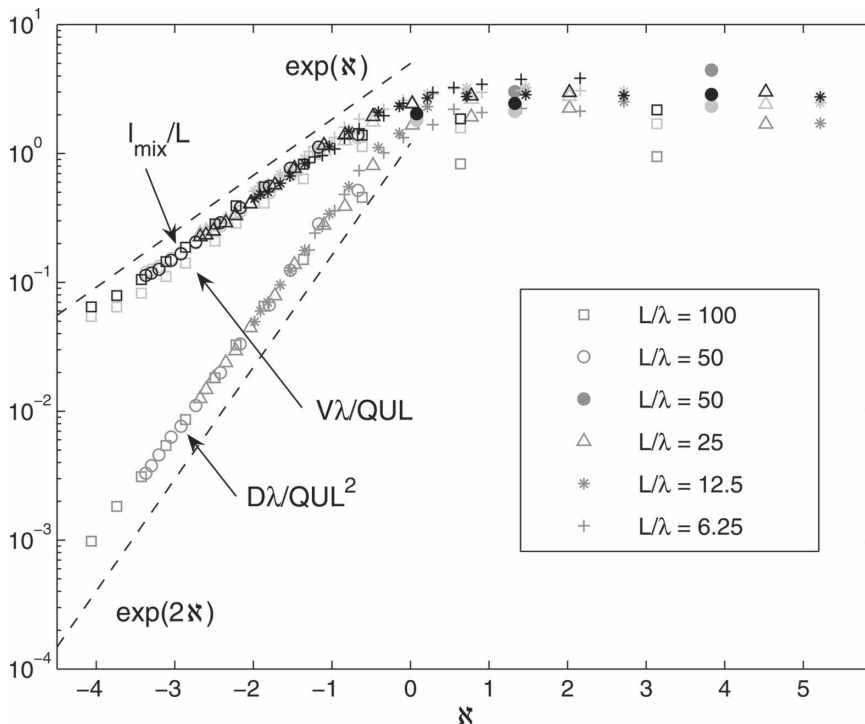
FIG. 11. According to the energy-balance relation and vortex-gas scaling, the local mixing regime is characterized by $V\lambda/QUL \approx \ell_{mix}/L \propto \exp(\aleph)$ and $(D\lambda/QUL^2) \propto \exp(2\aleph)$. These predictions are confirmed above by the collapse of the data to straight lines in the local regime where $\aleph < 0$. In addition, $\aleph$ also collapses the data in the global regime where $\aleph > 0$. The variable $\aleph$ is defined in (36), and the function $Q(\kappa_*)$ in (27).

major properties of this dilute vortex gas are exponentially sensitive to the bottom drag.

7. Resolution and hyperviscosity

To prevent the buildup of enstrophy at small scales, it is necessary to include dissipative term acting selectively on high wavenumbers. Arbic and Flierl (2003, 2004b) have shown that geostrophic turbulence simulations do not depend strongly on the form of this small-scale dissipation, for example, hyperviscosity or wavenumber filter. Regardless of form, though, the dissipation of energy due to this term should be relatively small.

In our simulations, we follow LH95 and use a hyperviscous term of the form ∇^8 (see appendix A). The rationale for this high-order operator is that it limits dissipation to the very largest wavenumbers, and leaves as much spectral room as possible for the direct enstrophy cascade. To compare our results with those reported in LH95 we repeated their main experiment—namely, experiment I—which has the following parameters:

$$\frac{L}{\lambda} = 50, \frac{\kappa\lambda}{U} = 0.08, \frac{\nu}{UL^7} = 1.024 \times 10^{-13}, \quad \text{and} \quad nn = 256^2.$$

Above, nn is the number of grid points.

In this simulation, 22.2% of the total energy extracted from the mean flow in the statistically steady state was balanced by the hyperviscous term hypν in (A10) and (A11). In LH95 hyperviscosity contributed to 19.9% of the dissipation; this discrepancy is most likely due to differences in the Ekman dissipation term in the layer and modal formulations. However, in a simulation where L/λ was reduced to a value of 25, with $\kappa\lambda/U$, ν/UL^7 and nn remaining fixed, the hyperviscous dissipation dropped to 7.13%.

This latter simulation has a finer resolution per deformation radius. In other words, given the same number of grid points, the flow is better resolved for smaller values of L/λ. We found that the resolution is at least as important as the actual coefficient of hyperviscosity, ν, in determining hypν. Table 1 gives an overview of the various small-scale dissipative parameters used in this study, and Fig. 12a shows Ekman dissipation ε_{Ekman} divided by total dissipation ε_{total} (Ekman and hyperviscous) for all the simulations. It is reassuring to see that

TABLE 1. Overview of small-scale dissipation parameters in all of the simulations. The symbols corresponding to each group of simulations are the same in all figures. The number of grid points per deformation radius was determined by taking the number of grid points on one side of the domain and dividing by $2\pi L/\lambda$.

Symbol	L/λ	ν/UL^7	Grid points	Grid points/λ
+	6.25	2.048×10^{-13}	128^2	3.26
*	12.5	2.048×10^{-13}	128^2	1.63
×	12.5	6.55×10^{-12}	128^2	1.63
△	25.0	1.024×10^{-13}	256^2	1.63
○	50.0	1.024×10^{-13}	512^2	1.63
●	50.0	1.024×10^{-13}	256^2	0.815
□	100.0	1.60×10^{-15}	512^2	0.815

as the resolution increases, the hyperviscous contribution decreases.

In our earliest large-domain simulations (i.e., $L/\lambda = 100$ with nn $= 512^2$ and $L/\lambda = 50$ with nn $= 256^2$), the hyperviscous energy dissipation was roughly 20%–30%

of the total. We regard this as an uncomfortably large contribution from the hyperviscosity. Thus, we performed a second series at $L/\lambda = 50$, doubling the resolution to nn $= 512^2$. The hyperviscous parameter ν was also reduced as the resolution was increased as described in Table 1. Within the global mixing regime, smaller times steps are necessary for stability and a longer averaging time is necessary to remove turbulent fluctuations. This computational burden prevented the four global mixing runs from being completed at 512^2 and so the comparison is limited to the local mixing regime. Comparing the filled circles with the open circles in Fig. 12a shows that increasing the resolution to 512^2 drops the hyperviscous energy dissipation considerably.

Other quantities are also sensitive to resolution. One example of this is the correlation coefficient c. Simulations with a fine resolution show that c is approximately constant and equal to 1/4 in the local mixing regime. Values of c for the reduced resolution sequences with
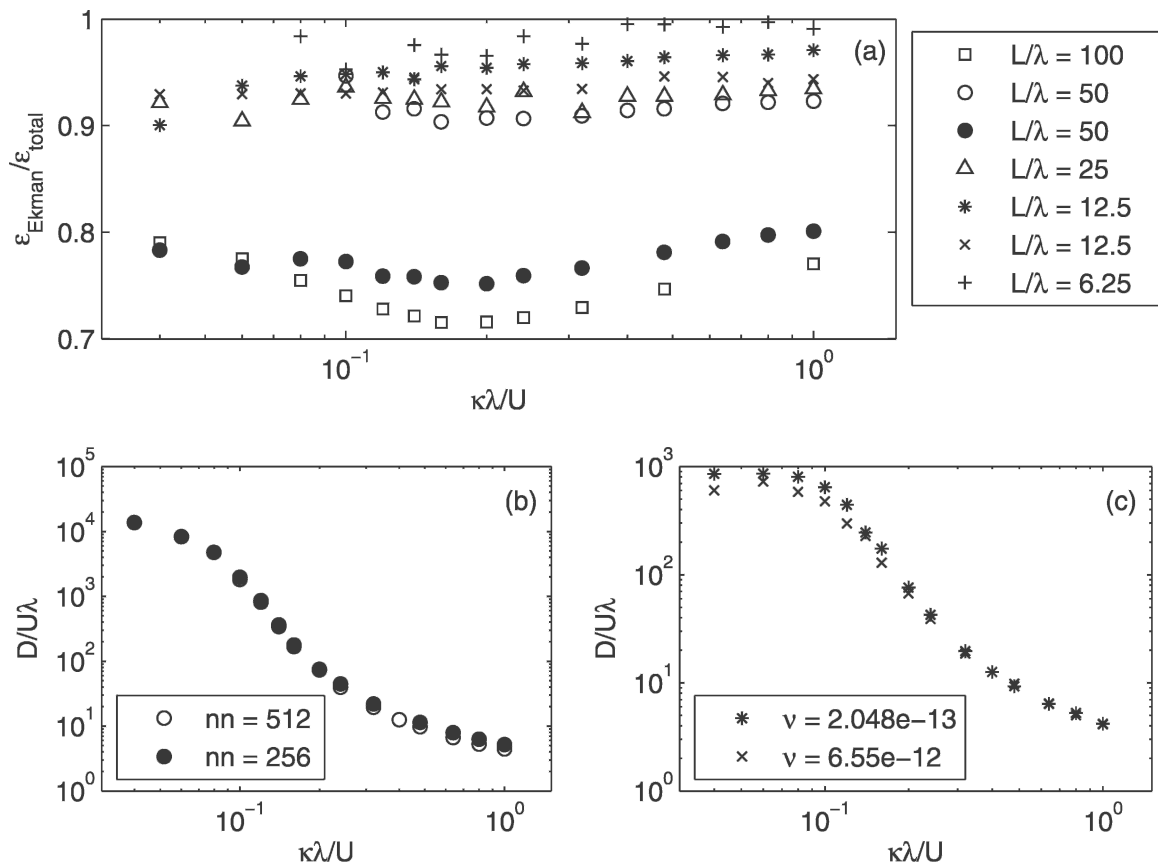

FIG. 12. (a) The ratio of the dissipation due to Ekman drag to the total dissipation (Ekman and hyperviscous). The two circle experiments ($L/\lambda = 50$) have different resolutions: 512^2 (open circles) and 256^2 (filled circles). Two series of simulations with $L/\lambda = 12.5$ were completed with different values of ν: 2.048×10^{-13} (asterisks) and 6.55×10^{-12} (times signs). (b) Values of D for runs with $L/\lambda = 50$. (c) Values of D with $L/\lambda = 12.5$.

$L/\lambda = 100$ and 50 collapsed onto a single curve with values between 0.27 and 0.37 in the local regime (not shown). This systematic variation due to insufficient resolution was limited to data within the local mixing regime. This led us to omit data for simulations with $L/\lambda = 100$ for some plots. Also, in Fig. 8a, $\langle \zeta^2 \rangle$ is shown to be sensitive to simulation resolution.

Considering the effect resolution has on hypν, c, $\varkappa_1$, and other properties, it is somewhat surprising that varying resolution makes only a small change in D. Figure 12b compares the values of D for the two series with $L/\lambda = 50$. All the simulations in the local mixing regime have been performed at both resolutions, and the values of D are so similar that it is difficult to distinguish the filled circles from the open circles in Fig. 12b. This result gives us confidence in our $L/\lambda = 100$ results for D despite the large hyperviscous energy dissipation in this sequence (Fig. 12a).

As a further test, Fig. 12c shows that varying ν at fixed resolution has a small effect on D. Figure 12c shows two sequences (marked with asterisks and times signs, respectively) with $L/\lambda = 12.5$ and $\nu_\times = 32\nu_*$, with nn $= 128^2$ in both cases. Again, the large change in ν has little impact on D, especially in the local mixing regime. In the global regime, there is a systematic decrease in D for the simulations with increased hyperviscosity. This discrepancy may be due to the fact that the simulations with increased ν spin up faster, and are also less volatile.

8. Discussion and conclusions

In this article we have shown that the main predictions of the dual-cascade theory of equilibrated baroclinic turbulence on an f plane are inaccurate; for example, the ratios $Dk_0^2\lambda/U$ and $V\lambda/U\ell_{mix}$ are not constant. We have identified the underlying physical reasons for the failure of this theory, for example, the dominance of bottom drag in the large-scale barotropic vorticity equation in (32), and the prominence of coherent vortices. We have proposed an alternative theory for baroclinic eddy fluxes based on vortex-gas scaling (Carnevale et al. 1991) and energy balance. Animations of equilibrated simulations show that vortices persist and travel across the domain. The baroclinic heat flux is evident in these animations as a systematic tendency for hot anticyclonic vortices to move northward, and cold cyclonic vortices southward. However, a great difference from the barotropic problem studied by Carnevale et al. (1991) is that in the equilibrated state same-signed vortex merger is rare.

An important feature of the vortex theory is that there are at least four relevant length scales. In the local regime these four adhere to the relationships

$$\lambda < r_{core} \ll \ell_{mix} \ll L. \tag{41}$$

Scale separation between L and ℓ_{mix} is necessary for the validity of diffusive parameterizations, but there is also an important scale separation between ℓ_{mix} and r_{core}. In section 3, we showed that the diffusivity D depends on both the mixing length and the core radius through

$$D \sim \frac{U\ell_{mix}^2 r_{core}}{\lambda^2}. \tag{42}$$

In section 4, the mechanical energy Eq. (2) is used to express ℓ_ζ (and therefore r_{core}) in terms of $\kappa\lambda/U$; for example, see (26). And in section 6 we proposed an empirical expression for ℓ_{mix} in terms of $\kappa\lambda/U$; for example, see (38). The exponential sensitivity of ℓ_{mix} to $\kappa\lambda/U$ enters through this empirical relation, but a compelling physical explanation for this exponential relation has eluded us. We believe that the answer is again related to the long-lived coherent vortices that dominate the flow. A full understanding of homogeneous quasigeostrophic turbulence on an f plane will require an analysis of how these coherent structures are created, how they work to halt the linear baroclinic instability, and how they interact in statistical equilibrium.

Of course, introduction of a planetary potential vorticity gradient, β, would make this model more applicable to the ocean and also provide a mechanism for halting, without damping, the inverse cascade and suppressing vortices. Held and Larichev (1996) and Lapeyre and Held (2003) have shown that β can indeed halt the inverse cascade, and they have presented scalings for the diffusive flux again applying the dual-cascade model. Danilov and Gurarie (2002) have presented barotropic simulations that include both bottom friction and β, and have documented a transition between friction-dominated and β-dominated regimes. Still, an understanding of how these two mechanisms influence the eddy fluxes and the formation of coherent structures is incomplete. This will be one focus of a forthcoming study based on a new suite of simulations that include the effects of β and bottom friction. Preliminary results suggest that coherent structures can be prominent features even in simulations with moderate values of β. Thus, the work presented here lays a foundation for understanding the role of coherent structures and eddy fluxes that will apply to more realistic models.

APPENDIX A

The Two-Mode Equations of Motion

The derivation of the modal equations used in our study is based on Flierl (1978), and also includes forcing terms that arise when there is a mean shear in the basic state as discussed in Hua and Haidvogel (1986). Our equations differ from those of Hua and Haidvogel only in the form of the hyperviscous term, which is used to absorb enstrophy cascading to the highest wavenumbers. The main difference between the modal decomposition used here and the method used by Larichev and Held (1995) appears in the coefficients of the bottom drag term as shown below.

The continuous quasigeostrophic equations are written as

$$\frac{\partial}{\partial t} Q + J(\Psi, Q) = -\nu\nabla^8 Q. \qquad (A1)$$

Here J represents the Jacobian, $J(a, b) \equiv a_x b_y - a_y b_x$, Ψ is the streamfunction such that $u = -\Psi_y$ and $v = \Psi_x$, and

$$Q = \nabla^2\Psi + (f/N)^2\Psi_{zz} \qquad (A2)$$

is the potential vorticity. We consider dynamics on an f plane, and take the Brunt–Väisälä frequency N to be constant. The coefficient of hyperviscosity is given by ν and H is the depth of the ocean. We then define the first Rossby radius of deformation as

$$\lambda = \frac{NH}{\pi}. \qquad (A3)$$

Using a truncated modal expansion in the vertical, we consider the barotropic and first baroclinic modes in the presence of a mean shear. We write this as

$$\Psi(x, y, z, t) = \psi(x, y, t)$$
$$+ [-Uy + \tau(x, y, t)]\sqrt{2}\cos\left(\frac{\pi z}{H}\right), \qquad (A4)$$

where ψ and τ are the perturbation streamfunctions of the barotropic and baroclinic modes, respectively. The factor of $\sqrt{2}$ arises from normalization of the modes (Flierl 1978). The potential vorticity written in terms of this modal expansion is

$$Q = \nabla^2\psi + (\nabla^2\tau - \lambda^{-2}\tau + U\lambda^{-2}y)\sqrt{2}\cos\left(\frac{\pi z}{H}\right). \qquad (A5)$$

We now apply the modal decomposition of Ψ to the quasigeostrophic equation and project in the barotropic and baroclinic modes. The frictional, or Ekman drag, terms arise from the bottom boundary condition:

$$w(x, y, -H, t) = \delta_E\nabla^2\Psi(x, y, -H, t), \qquad (A6)$$

where δ_E is the Ekman layer depth. In our model the Ekman drag coefficient is defined by $\kappa = f\delta_E/H$.

The modal equations are

$$\nabla^2\psi_t + J(\psi, \nabla^2\psi) + J(\tau, \nabla^2\tau) + U\nabla^2\tau_x = -\kappa\nabla^2(\psi - \sqrt{2}\tau)$$
$$- \nu\nabla^8(\nabla^2\psi) \qquad (A7)$$

and

$$(\nabla^2 - \lambda^{-2})\tau_t + J[\psi, (\nabla^2 - \lambda^{-2})\tau] + J(\tau, \nabla^2\psi)$$
$$+ U(\nabla^2 + \lambda^{-2})\psi_x = -\kappa\nabla^2(2\tau - \sqrt{2}\psi)$$
$$- \nu\nabla^8(\nabla^{-2} - \lambda^{-2})\tau. \qquad (A8)$$

Nondimensionalizing lengths with the deformation length λ and time with λ/U gives the three nondimensional parameters in the system:

$$\frac{\lambda}{L}, \frac{\kappa\lambda}{U}, \quad\text{and}\quad \frac{\nu}{U\lambda^7}. \qquad (A9)$$

The energy balance is obtained in the standard manner by multiplying the barotropic and baroclinic modal equations by ψ and τ, respectively, and ensemble averaging. In a statistically steady state the energy balance requires

$$U\lambda^{-2}\langle\psi_x\tau\rangle = \kappa\langle|\boldsymbol{\nabla}\psi - \sqrt{2}\boldsymbol{\nabla}\tau|^2\rangle + \text{hyp}\nu, \qquad (A10)$$

where the hyperviscous term is given by

$$\text{hyp}\nu = \nu\langle|\nabla\nabla^4\psi|^2\rangle + \nu\langle|\nabla\nabla^4\tau|^2\rangle + \nu\lambda^{-2}\langle(\nabla^4\tau)^2\rangle. \qquad (A11)$$

APPENDIX B

Vortex Census Algorithm

The automated vortex census algorithm primarily follows the method outlined in McWilliams (1990) to identify vortices in a two-dimensional gridded vorticity field at a given time. The method begins by identifying

all points above a vorticity threshold value ζ_{min}. Following McWilliams (1990), this value is taken to be 5% of the maximum vorticity magnitude in the field. The vortices are also required to have a vorticity extrema at their centers. Thus, any point whose magnitude is smaller than one or more of its surrounding points is also excluded. Because we are interested in counting axisymmetric structures, we added a further constraint based on the Okubo–Weiss parameter (Okubo 1970, Weiss 1991), which measures the relative importance of vorticity versus strain. The Okubo–Weiss parameter is

$$OW = s_n^2 + s_s^2 - \zeta^2 = 4(u_x^2 + u_y v_x), \qquad (B1)$$

where $s_n = u_x - v_y$ is the normal component of strain and $s_s = u_y + v_x$ is the shear component of strain. The Okubo–Weiss parameter is negative when rotation dominates and positive when strain dominates. Therefore, we require that the Okubo–Weiss parameter at the center of each of our vortices be negative and have a magnitude larger than a threshold OW_{min}. Similar to the vorticity we take OW_{min} to be 5% of the maximum OW magnitude in the field (the value of OW at the point of maximum magnitude is always negative).

The boundary of each vortex is determined following the method in McWilliams (1990), which traces a counterclockwise path around the boundary based on a vorticity threshold. Using the boundary to measure r_{core} proved to be difficult since not all vortices are perfectly axisymmetric and many vortices only have a core radius of three to four grid points. We found that a more effective method for determining an average vortex radius was to count all the points that had a negative value of OW and a magnitude greater than OW_{min}. Considering the physical fields, these points were found to lie almost exclusively inside the vortex cores. Dividing the number of points that satisfy the OW threshold by the number of vortices in that particular snapshot provides an estimate of the area of an average vortex (this is not the true area since we are only counting points). From observations of the physical fields, the square root of this number was found to agree well with a typical core radius and was taken as the value for r_{core} in Fig. 9b.

Simulations with $L/\lambda = 25$ and $\kappa\lambda/U = (0.16, 0.24, 0.32, 0.48, 0.64, 0.80)$ were run for a time $tU/\lambda = 125$ in the equilibrated state during which 50 snapshots of barotropic vorticity and the Okubo–Weiss parameter of the barotropic mode were saved. The vortex census was completed for each snapshot and the values for N and r_{core} plotted in Fig. 9 are the mean of these 50 realizations. The values for ζ_{min} and OW_{min} were varied systematically. These changes alter the resulting values of

N and r_{core}, but the relationship between different values of bottom drag does not change significantly. For example, changes in threshold values cause the slope in Fig. 9a to vary between -0.52 and -0.62.

REFERENCES

Arbic, B. K., and G. R. Flierl, 2003: Coherent vortices and kinetic energy ribbons in asymptotic, quasi two-dimensional f-plane turbulence. *Phys. Fluids,* **15,** 2177–2189.

——, and ——, 2004a: Baroclinically unstable geostrophic turbulence in the limits of strong and weak bottom Ekman friction: Application to midocean eddies. *J. Phys. Oceanogr.,* **34,** 2257–2273.

——, and ——, 2004b: Effects of mean flow direction on energy, isotropy, and coherence of baroclinically unstable beta-plane geostrophic turbulence. *J. Phys. Oceanogr.,* **34,** 77–93.

Carnevale, G. F., J. C. McWilliams, Y. Pomeau, J. B. Weiss, and W. R. Young, 1991: Evolution of vortex statistics in two-dimensional turbulence. *Phys. Rev. Lett.,* **66,** 2735–2737.

Danilov, S., and D. Gurarie, 2002: Rhines scale and spectra of the β-plane turbulence with bottom drag. *Phys. Rev.,* **65E,** R067301, doi:10.1103/PhysRevE.65.067301.

Flierl, G. R., 1978: Models of vertical structure and the calibration of two-layer models. *Dyn. Atmos. Oceans,* **2,** 342–381.

Green, J. S. A., 1970: Transfer properties of the large-scale eddies and the general circulation of the atmosphere. *Quart. J. Roy. Meteor. Soc.,* **96,** 157–185.

Haidvogel, D. B., and I. M. Held, 1980: Homogeneous quasigeostrophic turbulence driven by a uniform temperature gradient. *J. Atmos. Sci.,* **37,** 2644–2660.

Held, I. M., and V. D. Larichev, 1996: A scaling theory for horizontally homogeneous, baroclinically unstable flow on a beta plane. *J. Atmos. Sci.,* **53,** 946–952.

Hua, B. L., and D. B. Haidvogel, 1986: Numerical simulations of the vertical structure of quasi-geostrophic turbulence. *J. Atmos. Sci.,* **43,** 2923–2936.

Lapeyre, G., and I. M. Held, 2003: Diffusivity, kinetic energy dissipation, and closure theories for the poleward eddy heat flux. *J. Atmos. Sci.,* **60,** 2907–2916.

Larichev, V., and I. Held, 1995: Eddy amplitudes and fluxes in a homogeneous model of fully developed baroclinic instability. *J. Phys. Oceanogr.,* **25,** 2285–2297.

McWilliams, J. C., 1990: The vortices of two-dimensional turbulence. *J. Fluid Mech.,* **219,** 361–385.

Okubo, A., 1970: Horizontal dispersion of floatable particles in the vicinity of velocity singularities such as convergences. *Deep-Sea Res.,* **17,** 445–454.

Pavan, V., and I. M. Held, 1996: The diffusive approximation for eddy fluxes in baroclinically unstable jets. *J. Atmos. Sci.,* **53,** 1262–1272.

Pedlosky, J., 1983: The growth and decay of finite-amplitude baroclinic waves. *J. Atmos. Sci.,* **40,** 1863–1876.

Rhines, P. B., 1977: The dynamics of unsteady currents. *The Sea,* E. A. Goldberg et al., Eds., Marine Modeling, Vol. 6, Wiley and Sons, 189–318.

Riviere, P., and P. Klein, 1997: Effects of an asymmetric friction on the nonlinear equilibration of a baroclinic system. *J. Atmos. Sci.,* **54,** 1610–1627.

——, A. M. Treguier, and P. Klein, 2004: Effects of bottom friction on nonlinear equilibration of an oceanic baroclinic jet. *J. Phys. Oceanogr.,* **34,** 416–432.

Salmon, R., 1978: Two-layer quasigeostrophic turbulence in a simple special case. *Geophys. Astrophys. Fluid Dyn.,* **10,** 25–52.

——, 1980: Baroclinic instability and geostrophic turbulence. *Geophys. Astrophys. Fluid Dyn.,* **15,** 167–211.

Smith, K. S., and G. K. Vallis, 2002: The scales and equilibration of midocean eddies: Forced-dissipative flow. *J. Phys. Oceanogr.,* **32,** 1699–1720.

Stone, P. H., 1972: A simplified radiative-dynamical model for the static stability of rotating atmospheres. *J. Atmos. Sci.,* **29,** 11–37.

Weiss, J., 1991: The dynamics of enstrophy transfer in two-dimensional hydrodynamics. *Physica D,* **48,** 273–294.